

# Interplay between cellular activity and three-dimensional scaffold-cell constructs with different foam structure processed by electron beam melting

Krishna C. Nune,<sup>1</sup> R. Devesh K. Misra,<sup>1</sup> Sara M. Gaytan,<sup>2</sup> Lawrence E. Murr<sup>2</sup>

<sup>1</sup>Biomaterials and Biomedical Engineering Research Laboratory, Center for Structural and Functional Materials, Institute for Materials Research and Innovation, University of Louisiana at Lafayette, Lafayette, Louisiana 70504

<sup>2</sup>Department of Metallurgical and Materials Engineering, The University of Texas at El Paso, El Paso, Texas 79968

Received 5 July 2014; accepted 31 July 2014

Published online 19 August 2014 in Wiley Online Library (wileyonlinelibrary.com). DOI: 10.1002/jbm.a.35307

**Abstract:** The cellular activity, biological response, and consequent integration of scaffold-cell construct in the physiological system are governed by the ability of cells to adhere, proliferate, and biomineralize. In this regard, we combine cellular biology and materials science and engineering to fundamentally elucidate the interplay between cellular activity and interconnected three-dimensional foamed architecture obtained by a novel process of electron beam melting and computational tools. Furthermore, the organization of key proteins, notably, actin, vinculin, and fibronectin, involved in cellular activity and biological functions and relationship with the structure was explored. The interconnected foamed structure with ligaments was favorable to cellular activity that

includes cell attachment, proliferation, and differentiation. The primary rationale for favorable modulation of cellular functions is that the foamed structure provided a channel for migration and communication between cells leading to highly mineralized extracellular matrix (ECM) by the differentiating osteoblasts. The filopodial interaction amongst cells on the ligaments was a governing factor in the secretion of ECM, with consequent influence on maturation and mineralization. © 2014 Wiley Periodicals, Inc. *J Biomed Mater Res Part A* 103A: 1677–1692, 2015.

**Key Words:** Ti-6Al-4V alloy, osteoblast functions, foamed structure, mineralization

**How to cite this article:** Nune KC, Misra RDK, Gaytan SM, Murr LE. 2015. Interplay between cellular activity and three-dimensional scaffold-cell constructs with different foam structure processed by electron beam melting. *J Biomed Mater Res Part A* 2015;103A:1677–1692.

## INTRODUCTION

Titanium alloys have been widely used since World War II to manufacture orthopedic implants.<sup>1,2</sup> The underlying reasons are high specific strength, low stiffness, excellent corrosion resistance in the physiological environment.<sup>1,2</sup> However, their usage as solid implants has serious limitations in many orthopedic devices and is primarily related to the biomechanical mismatch between the artificial medical device and the surrounding tissue. The biomechanical mismatch is responsible for the stress-shielding that introduces undesirable distribution of stress at the bone tissue-implant interface.<sup>3</sup> Taking into consideration the elastic modulus of titanium alloys ~90–115 GPa, the biomechanical mismatch is at least one order greater in relation to cortical hard bone (outer region of femoral and tibial bones: 16–20 GPa) and up to two orders of magnitude for the inner (medullary) cancellous or trabecular soft bone with open cellular structure, which has modulus an order of magnitude lower than the cortical bone.<sup>4–6</sup> The detrimental effect of the biomechanical mismatch is delayed bone healing, which is also nonuniform in a majority of the cases.<sup>3</sup> Moreover, the bio-

mechanical mismatch renders load-bearing orthopedic implant stem devices nonpatient specific, such that the biomechanical mismatch is different from patient to patient, even if the orthopedic devices may have a porous coating on the surface to promote bone tissue ingrowth and increase the stability of the medical device.<sup>7–10</sup>

A viable and practical method to eliminate the disadvantage of biomechanical mismatch is to utilize three-dimensional (3D) porous foam or mesh structures with appreciable lower modulus than the solid alloy implant. Murr et al's group at the Keck Center for 3D Innovation at the University of Texas at El Paso successfully fabricated monolithic orthopedic device prototypes of titanium alloys with regular and interconnected foam and mesh arrays, and fully dense components by additive manufacturing (AM; layer-by-layer fabrication) from precursor powders using electron beam melting (EBM).<sup>11,12</sup> The foam and mesh structures included geometrical structures that were built in lattice-style, 3D periodic, reticulated geometry from the lattice elements or unit cell structures embedded in computer-aided design (CAD) software driving the AM-EBM process.<sup>12,13</sup>

**Correspondence to:** R. D. K. Misra; e-mail: dmisra@louisiana.edu

In addition to the benefit of bone resorption, there are other advantages associated with the use of 3D porous structures. They include superior cell-cell communications, cell-extracellular matrix (ECM) interactions, and high cell density. Moreover, the 3D porous structures are expected to be the driving force for efficient blood vessel ingrowth and enhanced oxygen, nutrient and waste flow/diffusion because of the porous nature of the implant architecture.<sup>14,15</sup> Recent studies with porous alginate hydrogels indicated significant albumin production of HepG2 cells.<sup>16</sup>

Motivated by the recent success in the fabrication of patient specific biomedical devices by AM that can potentially replace hard tissue, we elucidate here the biological response of 3D foam structures with different pore diameter, in terms of cell adhesion, intracellular and ECM production, and differentiation. The primary aim is to explore the practical viability and interplay between 3D printed structures and osteoblast functions as related to pore diameter and a relative comparison with fully dense or solid Ti-6Al-4V alloy, along with the use of tissue culture plate (TCP) as controls.

## EXPERIMENTAL PROCEDURE

### Material fabrication and characterization

The spherical powder particle size used to fabricate Ti-6Al-4V foam structures was in the range of ~50–100  $\mu\text{m}$ . We used an ARCAM-EBM system for the fabrication of foam structures, and the experimental parameters have been previously outlined.<sup>2</sup> The fabrication procedure utilized a structure generator that was constructed from a CT scan of a standard aluminum structure and used a materialize/magics software package to construct CAD models. In brief, atomized Ti-6Al-4V powder was used to build layers of ~100  $\mu\text{m}$  thick. The EBM system builds 3D-structures using the bottom-up approach by scanning the focused electron beam in a raster pattern to selectively melt specific areas of powder bed using a 3DCAD design system. During the process, the powder is continuously added from the powder cassettes to the top of the part or the structure being fabricated in vacuum. By changing beam current, scan rate, and heating schedules, the EBM system enables us to tune the microstructure in terms of porosity and pore size distribution along with control of mechanical properties (modulus, hardness etc.) in the final 3D structure. 3D foam structures of different pore size (see below) were fabricated.

The foam structures fabricated via the EBM system were qualitatively characterized by scanning electron microscopy (SEM) and quantitatively through a densitometry approach. The pore size was estimated from the SEM micrographs, whereas, porosity and modulus were calculated from densitometric measurements using the following equations:

$$\% \text{Porosity} = \left[ 1 - \left( \frac{\rho}{\rho_0} \right) \right] \times 100 \quad (1)$$

$$\text{Gibson-Ashby equation, } \frac{E}{E_0} = \left( \frac{\rho}{\rho_0} \right)^n \quad (2)$$

where  $E$  and  $E_0$  are the stiffness for an open-cellular structure and solid (fully dense) material having a density of  $\rho$  and  $\rho_0$ , respectively. For Ti-6Al-4V alloy,  $E_0 = 110$  GPa,  $\rho_0 = 4.43$  g/cc,  $n$  varies from ~1.8–2.2, and can be approximated to be 2.<sup>13</sup>

### Preosteoblast cell culture

Cell culture studies were performed using mouse preosteoblast MC3T3-E1 subclone four cell line obtained from American Type Cell Culture Collection (ATCC, Manassas, VA). Alpha minimum essential medium ( $\alpha$ -MEM, Invitrogen Corporation) supplemented with 10% fetal bovine serum, penicillin (100 U mL<sup>-1</sup>) and streptomycin (100  $\mu\text{g}$  mL<sup>-1</sup>) was used to culture preosteoblasts. Open cellular titanium alloy foam structures and flat and solid titanium alloy samples (1 cm<sup>2</sup>) were initially cleaned and sterilized by sonication for 1 h in ultrasonic bath containing soap water. After sonication, they were washed with acetone, isopropanol, ethanol, and deionized water. Next, the samples were sterilized in an autoclave and dried overnight. Preosteoblasts with 80–85% confluence obtained from T-flask cultures by trypsinization were used to seed onto the experimental samples. In brief, the cells were washed with phosphate buffer saline (PBS), incubated with 0.25% trypsin/0.53 mM EDTA for 5–7 min to detach the cells from T-flask, dispersed in trypsin/EDTA, transferred to a centrifuge tube and centrifuged at 2000 rpm for 5 min. Cell pellets obtained after centrifugation were resuspended in culture medium and dilution was carried out using the culture medium to obtain a defined cell density of 20,000 cells/well. Subsequently, the sterilized samples were placed in 24-well plates and incubated with cell suspension at 37°C in a humidified incubator with 5% CO<sub>2</sub> and 95% air. The controls used for comparison were fully dense and metallographically polished flat titanium alloy specimens and tissue culture polystyrene plates (TCP; Corning, IL).

### Seeding efficiency

Cellular titanium alloy foam structures and metallographically polished flat titanium alloy samples were seeded with preosteoblasts (20,000 cells/well) and incubated for 12 h at 37°C in a CO<sub>2</sub> incubator (5% CO<sub>2</sub> and 95% air) to examine cell seeding efficiency. After incubating for 12 h, the specimens were removed from their respective wells and the cells remaining in each well were stained with Trypan Blue and were counted using hemacytometer. The number of cells estimated from the hemacytometer was subtracted from the total number of initially seeded cells, to obtain the number of cells that were seeded on each specimen. The seeding efficiency was calculated using Eq. 3:

$$\% \text{ Seeding Efficiency} = \left( \frac{(\text{Total number of cells seeded}) - (\text{Cells attached to the well})}{\text{Total number of cells seeded}} \right) \times 100 \quad (3)$$

### Cell viability, attachment, and proliferation

Preosteoblasts (20,000 cells/well) seeded on open cellular foam structures and flat titanium alloy samples were incubated for 1, 2, and 6 h at 37°C in a CO<sub>2</sub> incubator (5% CO<sub>2</sub> and 95% air) to examine initial cell attachment/viability. For cell proliferation study, preosteoblasts (20,000 cells/well) were grown on surfaces for up to 14 days at 37°C in a CO<sub>2</sub> incubator. Culture medium was changed every 2–3 days for the duration of the experiment.

The initial cell attachment/viability and proliferation on open foam structure samples with varying porosity was measured using 3-(4,5-Dimethylthiazol-2-yl)-2,5-diphenyltetrazolium bromide (MTT) assay at predetermined times. The assay is based on the principle of reductase activity in mitochondria of living cells. The enzymes cleave the tetrazolium ring and turn the pale yellow MTT assay into dark blue formazan, whose concentration is proportional to the number of metabolically active cells. After predetermined incubation times, the samples were washed twice with PBS and incubated with fresh culture medium containing MTT (0.5 mg/mL medium) at 37°C for 4 h in the dark. Then, the unreacted dye was removed and dimethyl sulfoxide was added to dissolve the intracellular purple formazan product into a colored solution. The absorbance of this solution was quantified by spectrophotometer at 570 nm with a plate reader (Bio TEK Instrument, EL307C).

To further complement the MTT assay data, the cell-seeded samples were studied using fluorescence microscope (Nikon Eclipse E600 FN) after staining with the nucleic acid dye, 4',6-diamidino-2-phenylindole (DAPI). The cell-seeded samples after 14 d were washed twice with PBS and incubated with DAPI (1 µL dye/mL PBS) for 5 min at 25°C and viewed under fluorescence microscope with excitation and emission of 346/442 nm, respectively. The cell nuclei appear as blue spots in the fluorescence microscope.

### Immunofluorescence microscopy

The primary proteins that are engaged in cell adhesion are fibronectin, vinculin, and actin. These proteins were studied via immunofluorescence microscopy. The organization and distribution of vinculin-associated actin cytoskeleton and extracellular fibronectin of preosteoblasts was analyzed to understand the effect of porosity and pore interconnectivity on titanium alloy foam structures. The protocol that was adopted was as follows: preosteoblasts seeded on foam structures of different porosities were cultured for 14 days and used for immunostaining. The cell-seeded foam structure samples were washed twice with PBS, fixed with 4% paraformaldehyde for 20 min, permeabilized with 0.1% Triton X-100 for 5 min and blocked with 0.1% bovine serum albumin for 30 min. Next, immunocytochemistry staining was performed for fibronectin, actin, and vinculin expression.

Fibronectin was immunostained (labeled) with diluted mouse monoclonal antibody against fibronectin (1:800) (Sigma-Aldrich, St. Louis, MO) followed by rabbit-antimouse FITC conjugated secondary antibody at a working dilution of 1:200 (Sigma-Aldrich, St. Louis, MO). Then, cell nuclei were stained with DAPI (Chemicon International, Temecula, CA) at a working dilution of 1:1000 for 5 min. The actin

cytoskeleton and focal adhesion contacts were stained with a focal adhesion staining kit (Chemicon International, Temecula, CA). Actin and vinculin double staining was performed by incubating cells in diluted primary antibody (anti-vinculin) in blocking solution (1:200) for 1 h and subsequently labeled with diluted secondary antibody (1:100) (goat-anti-mouse FITC conjugate) (Chemicon International, Inc., Temecula, CA), for 45 min, and simultaneous incubation with diluted TRITC-conjugated phalloidin (1:400). Finally, cell nuclei were labeled with DAPI as described above. After immunostaining, samples were examined by fluorescence microscopy (Leica DM 6000B and Leica DM 600M).

### Cell morphology and adhesion

We used SEM to study the morphology, pore-interconnectivity, and in-growth of preosteoblasts, grown on samples for 7 d, 14 d, and 21 d. The cell-seeded samples were fixed with 2.5% glutaraldehyde in 0.1M cacodylate buffer pH 7.4 for 20 min, rinsed with PBS, dehydrated with a graded series of ethanol (25–100%) and critical point dried. Prior to examination of samples via SEM (Hitachi S-3000N), the samples were sputter-coated with 10 nm of gold.

The calcium-content in the ECM was estimated after 7, 14, and 21 days via energy dispersive X-ray analysis in the SEM. The ratio of calcium to phosphorous (Ca/P) was estimated and compared with natural hydroxyapatite (~1.67).

### Estimation of total protein content

At the end of each of preselected test durations (i.e., 7 d, 14 d, and 21 d), osteoblasts were lysed with 0.2% Triton X-100 for 30 min. Total protein content in the cell lysates was determined spectrophotometrically using Bradford protein assay kit. In brief, 25 µL of cell lysate was mixed with 400 µL of Bradford reagent and protein concentration estimated by measuring the absorbance/optical density at 570 nm on a Bio-Rad 550 spectrophotometric microplate reader. Total intracellular protein (expressed as mg) synthesized by osteoblasts cultured on 3D-foam structures and flat titanium alloy samples was determined from the standard plot of absorbance as a function of albumin concentration.

### Study of osteoblast differentiation by alkaline phosphatase activity

The cell lysate obtained after treating with 0.2% Triton X-100 was used to determine the alkaline phosphatase (ALP) activity, using ALP assay kit (QuantiChrom). The absorbance at 405 nm was measured via a spectrophotometer in a 96-well microplate reader (Bio-Rad 550). The ALP activity (expressed as micromoles of converted *p*-nitrophenol/min) was normalized by total intracellular protein synthesis (determined as described in the total intracellular protein content section 2 g and expressed as micromoles of *p*-nitrophenol per minute per milligram protein. ALP activity of osteoblasts cultured on flat titanium alloy and TCP served as controls.

### ECM mineralization—Alizarin red assay

The study of mineralization of ECM can be viewed as a measure or potential for bone formation. In this regard,



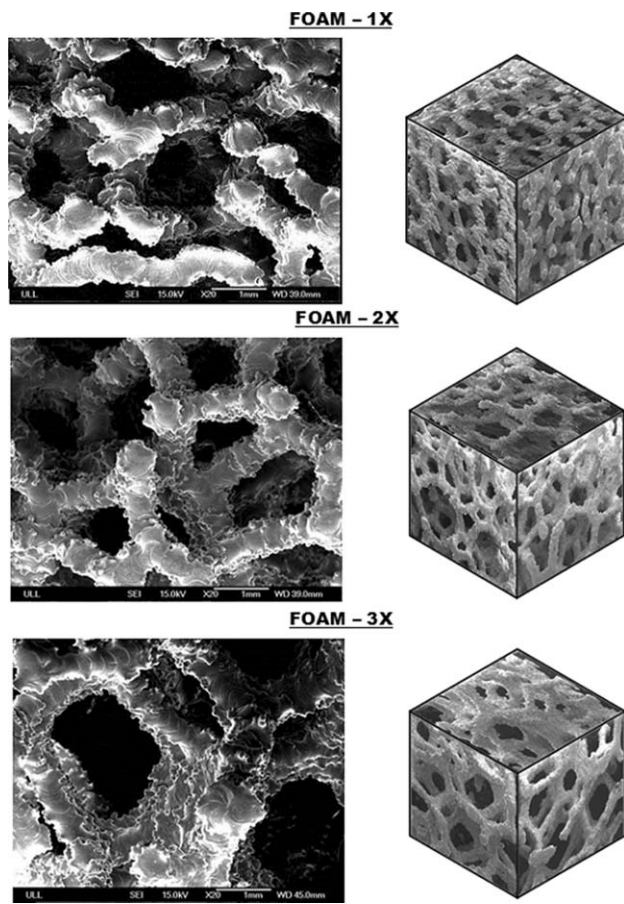


**FIGURE 1.** Two-dimensional and 3D representation of open cellular foam structure of Ti-6Al-4V alloy with different porosity (Foam 1X: porosity~76%, Foam 2X: porosity~86%, and Foam 3X: porosity~90%) as envisaged through SEM.

alizarin red assay (ARS) was qualitatively and quantitatively analyzed to indicate the presence of calcium in the matrix. Briefly, cells were seeded with osteoblast differentiation medium (Zen Bio) for 7, 14, and 21 days. After incubation, the samples were washed carefully with PBS without disturbing the cell layer and fixed with 4% paraformaldehyde for 30 min. The 3D foam structures were then stained with alizarin red (pH~4.1) in dark and at room temperature for 30 min. Samples were qualitatively studied via light microscope after rinsing with PBS. The calcium nodules appeared red. To conduct quantitative analysis, 10% cetyl pyridinium chloride was added to destain the alizarin red stain. The absorbance of the solution was measured at 570 nm OD with a spectrophotometric microplate reader.

#### Statistical analysis of data

The data was normalized with respect to control experiments and expressed as the mean of at least three replicates SD (standard deviation). Three sets of experiments were carried out for each experimental run. Statistical analysis was performed using a one way analysis of variance with 95% confidence interval.

## RESULTS

### Structural morphology of foam structures

In Figure 1, are presented two-dimensional (2D) and 3D representations of cellular foam structures of titanium alloy (Ti-6Al-4V) with different porosities, as imaged through SEM. The percentage porosity and modulus of the foam structures evaluated using Eqs. 1 and 2, respectively, are summarized in Table I. The pore size was in the range of 700–1500  $\mu\text{m}$  for the foam structures. The porosity and elastic modulus of foam titanium alloy structures was in the range 76–90% and 6–1 GPa, respectively. The elastic modulus of titanium alloy foam structure was comparable with the natural bone (cortical bone ~20 GPa and trabecular bone ~2 GPa).

### Seeding efficiency of cells, initial cell attachment/ viability, and cell proliferation

Preosteoblasts were seeded on titanium alloy foam structures together with solid titanium alloy at a density of 20,000 cells/well. Figure 2 shows that the seeding efficiency was reduced with increase in % porosity of titanium alloy foam structures (Table I) and the seeding efficiency was appreciably greater on solid titanium alloy, which is not surprising.

The early stages of cell attachment was studied in terms of cell metabolism and quantified via the approach of mitochondrial reduction of MTT up to 6 h. Here, the optical density is measure of metabolic activity. The results of such an analysis are presented in Figure 3(a). Figure 3(a) indicates that the number of cells attached to titanium alloy foam structures increased with time and followed a behavior identical to the solid titanium alloy and TCP. This implied the nontoxic nature of 3D foam structures, with the behavior being identical to the solid titanium alloy. It is interesting to note from Figure 3(a) that the degree of cell attachment with time (1, 2, and 6 h) as determined via optical density measurements was almost independent of pore size and % porosity, for the pore sizes studied here.

In Figure 3(b), is presented the cell proliferation data (0–21 days) that indicated an increase in metabolic activity until day 7 for all the samples. In comparison to the foam structures, the cellular activity was appreciably greater on TCP and flat Ti alloy at every time point, and the trend of cellular activity was similar on foam structures with different pore size. A superior indicator of cell proliferation is the

**TABLE I. Microstructural Parameters and Mechanical Properties of Three-Dimensional Titanium Alloy Foam Structures**

Sample ID	Density ( $\rho$ ), g/cc	Average Pore Size ( $\mu\text{m}$ )	% Porosity	Elastic Modulus (E), GPa
Foam – 1X	1.06	700	76.1	6.3
Foam – 2X	0.64	1000	85.6	2.3
Foam – 3X	0.43	1500	90.3	1.1

The porosity and elastic modulus were calculated using densitometry (Eq. 1) and Gibson-Ashby (Eq. 2). The pore size was determined from scanning electron micrographs (SEM).

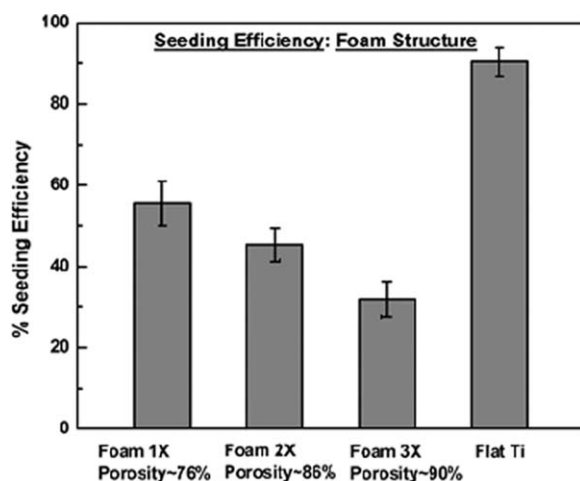


**FIGURE 2.** Histograms representing seeding efficiency for cellular Ti alloy-foam 3D structures after 12 h culture time (Foam 1X: porosity~76%, Foam 2X: porosity~86%, and Foam 3X: porosity~90%).

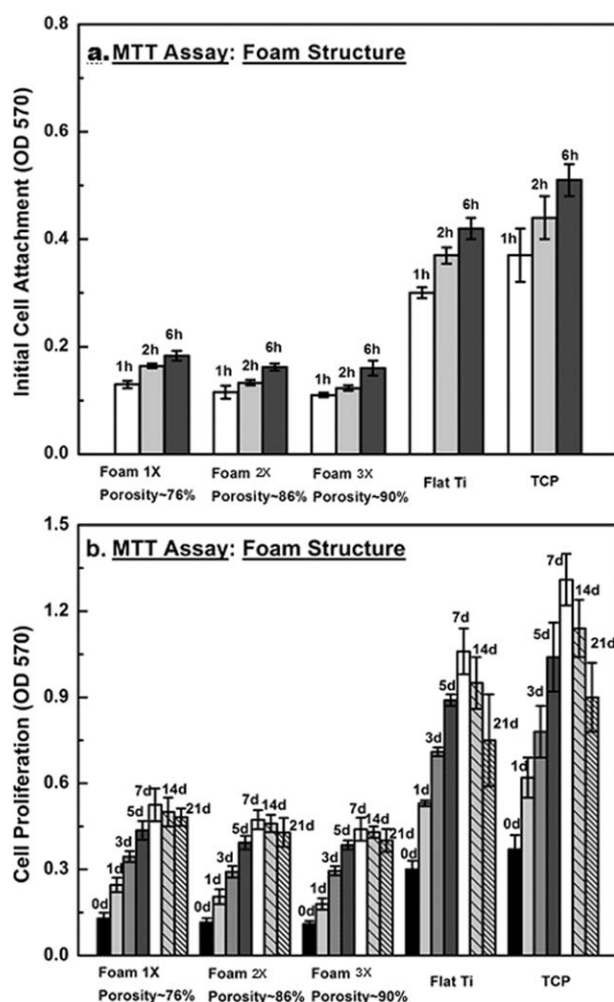


**FIGURE 3.** Histograms (a, b) representing initial cell attachment/viability, and cell proliferation of preosteoblasts after culture time of 1–6 h, and 0–21 d as studied by MTT assay for flat-Ti, TCP, and cellular Ti-foam 3D-structures of different porosity (Foam 1X: porosity~76%, Foam 2X: porosity~86%, and Foam 3X: porosity~90%).

proliferation rate. The proliferation rate (Fig. 4) expressed as the percentage increase in metabolic activity per day for the initial 1 through 7 day growth phase was significantly greater for foam structures, in comparison to the solid titanium alloy and TCP. The proliferation rate was in the range of ~42% for different foam structures. The data presented in Figure 4 suggested that proliferation rate was similar for different foam structures and was not governed when the % porosity is in the range of ~76–90%. Figure 3(b) also indicates that day 7 represent the transition period, after which the proliferation was decreased only to a very small extent for all the foam structures, while the decrease was greater for solid titanium alloy and TCP, which showed significantly higher proliferation. One can also say that proliferation on foam structures was stabilized at day 7.

The fluorescent micrographs after 14 days of culture and representing cell nuclei as blue spots (Fig. 5) provided a view of cell proliferation that took place on the ligaments of the porous structure.

### Immunocytochemistry

The primary proteins involved in cell adhesion are fibronectin, vinculin, and actin. An idea of these proteins can be obtained in terms of the expression level of proteins. The spread and proliferation of cells involves endogenous secretion of ECM proteins, such as fibronectin that directs cellular functions beyond initial adhesion. Vinculin expression and actin cytoskeleton (Fig. 6) expression were less significant on foam structures in striking comparison with the polished solid titanium alloy (control). High fluorescence intensity of ECM protein, fibronectin, and DAPI that stains nucleus (Fig. 7) was observed on foam structures. The individually stained nuclei were appreciably distinct in the high magnification fluorescence micrographs. Significant evidence

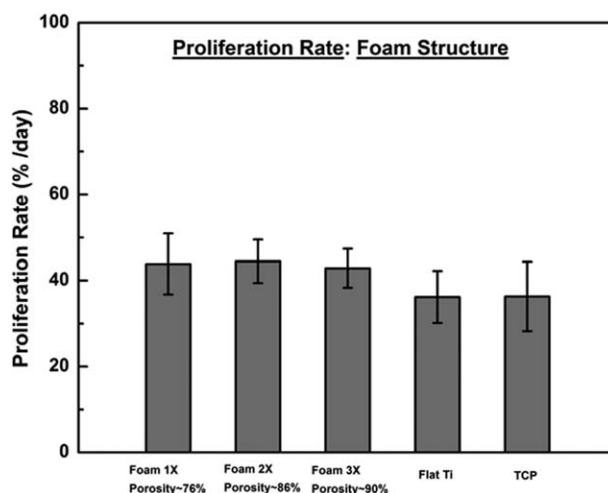


**FIGURE 4.** Histograms representing cell proliferation rates of preosteoblasts over the initial seven day growth phase on flat-Ti, TCP, and cellular Ti-foam 3D-structures of different porosity (Foam 1X: porosity~76%, Foam 2X: porosity~86%, and Foam 3X: porosity~90%). No significant difference in proliferation rate per day was observed for porous scaffolds, whereas nonporous control samples has lower proliferation rates as compared to porous scaffolds.

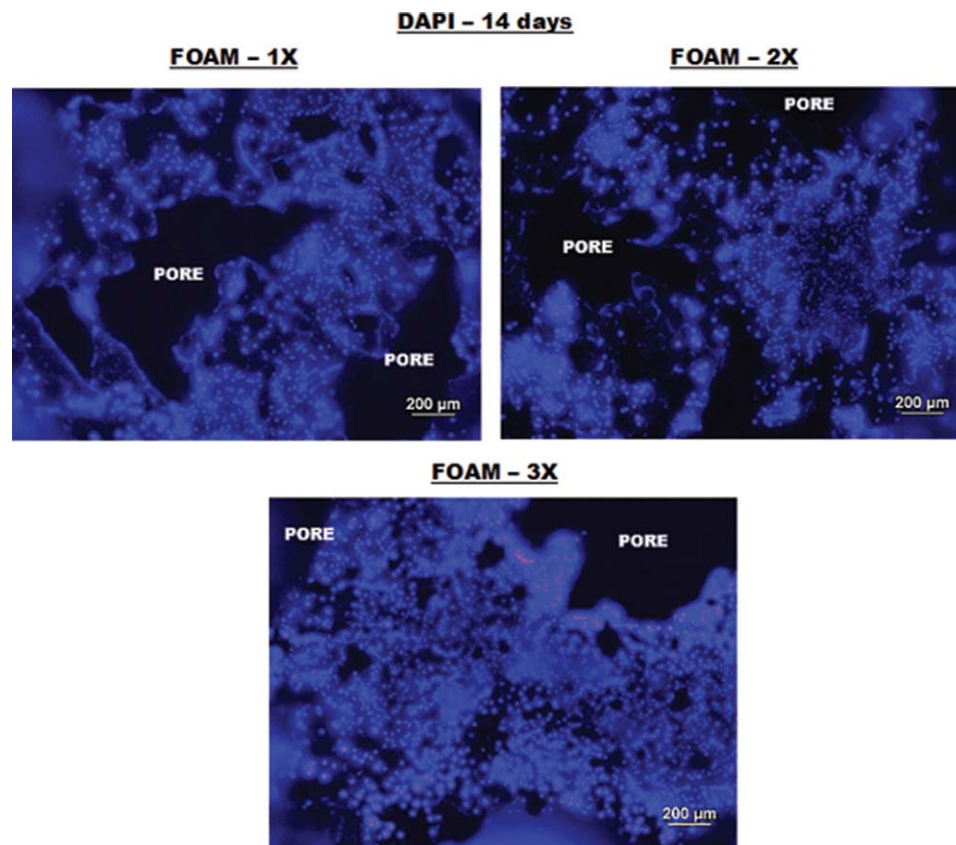


**FIGURE 5.** Fluorescent micrographs representing cell proliferation of preosteoblasts after 14 days of culture on cellular Ti-foam 3D-structures of different porosity (Foam 1X: porosity~76%, Foam 2X: porosity~86%, and Foam 3X: porosity~90%). Cell nuclei appear as blue fluorescence dots. [Color figure can be viewed in the online issue, which is available at [wileyonlinelibrary.com](http://wileyonlinelibrary.com).]

of protein expression in pores at day 14 implied that the cells proliferated through 3D extensions, gradually extending and filling the pores as spreading of cells occurred (see section Study of cell morphology: SEM). There was clear indication of ECM protein bridging the pores with the increase in the ECM protein.

#### Study of cell morphology: SEM

SEM micrographs illustrating morphology of cell spreading after day 7 are presented in Figures 8 and 9. The cells established bridges between the pores as evident from the elongated morphology (Fig. 8). With continued spreading of cells, a fibrous structure of ECM developed with cells wrapped and bridging the pores with their 3D filopodia extensions along the ligaments (Fig. 9). Considering that the cell spreading and growth within pores is dictated by the ability of the cells to bridge the pores with ECM, there was clear indication of a relationship between the pore size and cell proliferation, at least for the range of pore size of foam structures studied.

The ECM bridging the pores were observed at day 14 and beyond (21 days). Additionally, cells adhered to the surface and gradually filled the pores with continued spreading. The morphology of cells on foam structures during differentiation (after day 14) and mineralization phase (after day 21) as imaged via SEM are presented in Figures

10–13. These observations can be summarized as follows: The cells formed bridges between the pores with their elongated extensions (Fig. 10). Rough fibrous structures of ECM with cells embedded in the matrix were noted to wrap over the strut (Fig. 11). There were colonies of cells embedded in a confluent matrix, bridging the pores with their leading edges, at day 21 (Fig. 12). Dense ECM with mineralized nodules were present over the entire structure (Fig. 13). The above observations of mineralization of ECM were further confirmed via energy dispersive X-ray analysis in the SEM (Fig. 14). The increase in Ca/P ratio with increase in culture time until day 21 implied formation of bone-like apatite.

#### Monitoring of differentiation: ALP

The commencement of differentiation was studied via ALP enzyme activity (Fig. 15). The enzyme activity corresponding to the initial stage of differentiation marker on foam structures was significantly higher than on nonporous titanium alloy and TCP at every time point until day 14. However, the general behavior was similar on foam structures with different pore size. The ALP enzyme activity was observed to increase until day 14, followed by an appreciable decrease at day 21. In contrast, ALP enzyme activity on TCP and nonporous solid Ti alloy showed a continuous increase throughout the entire duration of test, and no decrease was noted at day 21, in contrast to porous foam



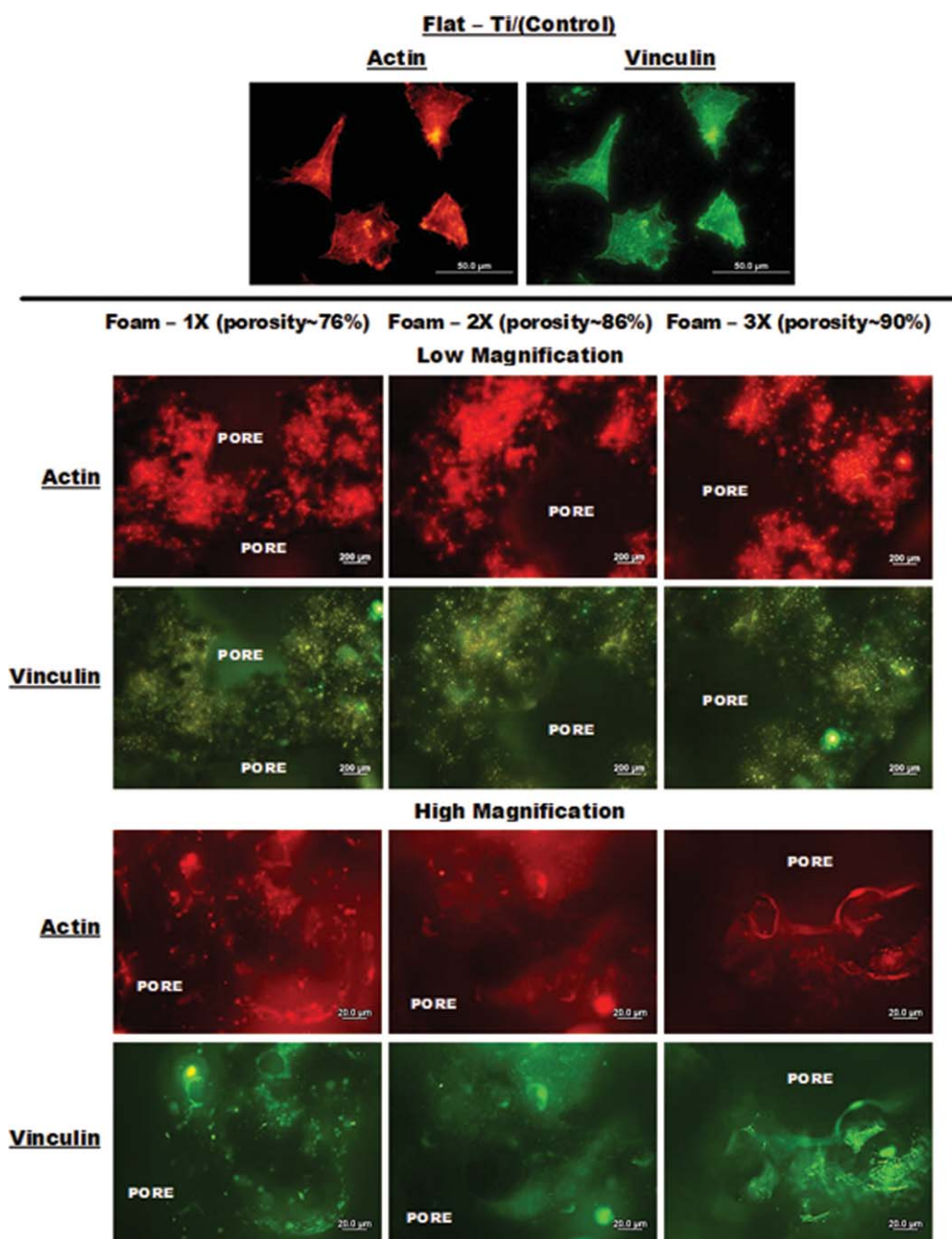


**FIGURE 6.** Low and high magnification fluorescence micrographs illustrating the organization and assessment of actin cytoskeleton (red) and vinculin focal contacts (green) of preosteoblasts cultured for 14 days on flat-Ti (control) and cellular Ti-foam 3D-structures of different porosity (Foam 1X: porosity~76%, Foam 2X: porosity~86%, and Foam 3X: porosity~90%). [Color figure can be viewed in the online issue, which is available at [wileyonlinelibrary.com](http://wileyonlinelibrary.com).]

structures. It was difficult to discuss the relationship between pore size, structure, and ALP activity for the different foam structures.

#### ECM mineralization

ARS was used to qualitatively and quantitatively study matrix mineralization of differentiated osteoblasts. Light micrographs of ARS-stained osteoblasts are presented in Figures 16–18. They indicate calcium-specific mineralized nodules on

3D-porous Ti-alloy foam structures with different porosity. The light micrographs presented in Figures 16–18 were stacked in three dimensions at different focal planes. Osteogenic supplements were provided by the osteoblast differentiation medium. At day 7, some mineral deposits of near monolayer coverage were detected on all the foam structures. Red color regions on the foam structures depicting calcium-enriched zones were observed to be greater after 14 days (Fig. 17) and 21 days (Fig. 18) of culture time, in comparison

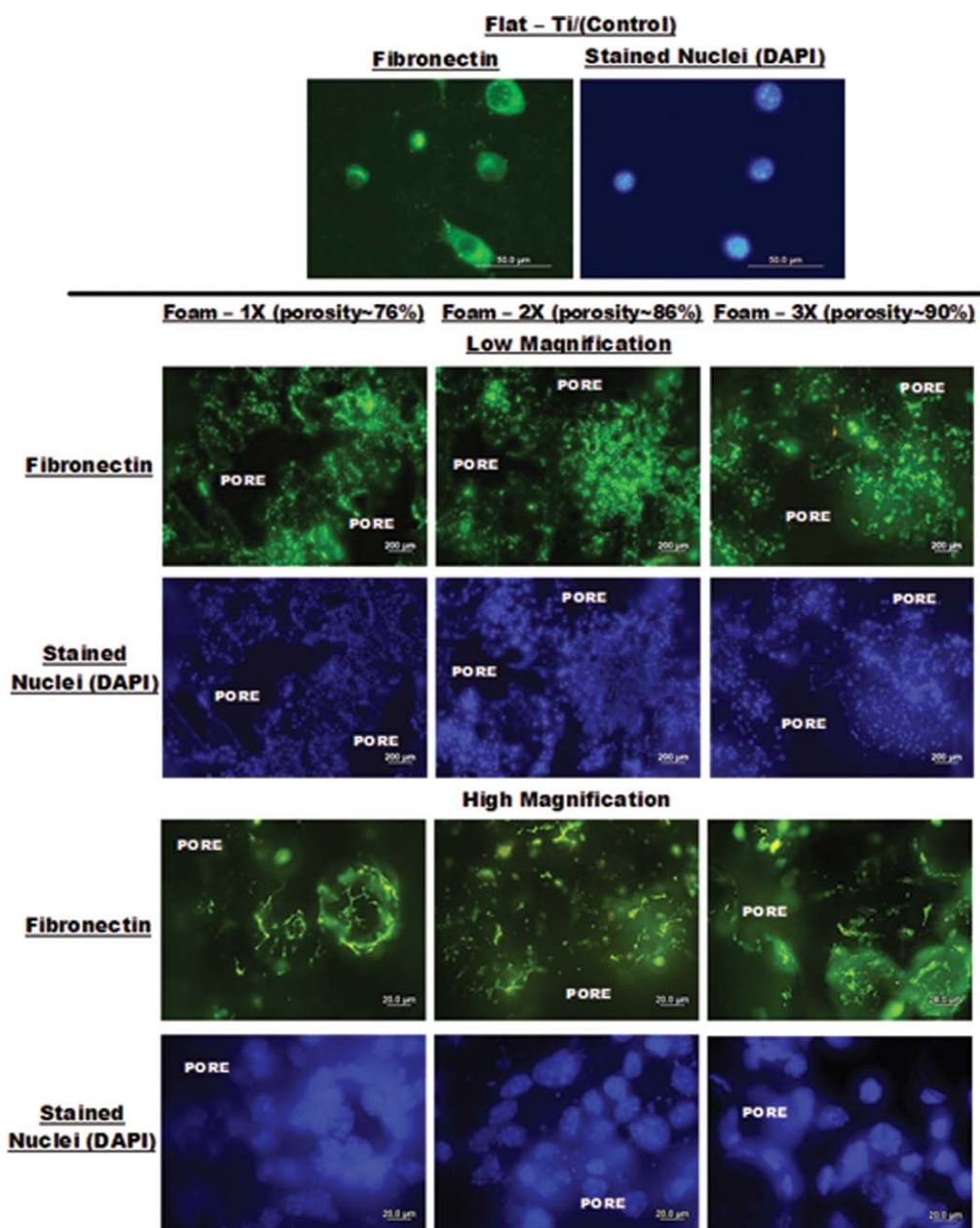


**FIGURE 7.** Low and high magnification fluorescence micrographs representing immunocytochemistry of fibronectin (green) and cell nuclei (blue) expressed by preosteoblasts after incubation for 14 days on flat-Ti (control) and cellular Ti-foam 3D-structures of different porosity (Foam 1X: porosity~76%, Foam 2X: porosity~86%, and Foam 3X: porosity~90%). [Color figure can be viewed in the online issue, which is available at [wileyonlinelibrary.com](http://wileyonlinelibrary.com).]

to 7 days. After 14 and 21 days, the mineral deposits were strongly stained and the nodules appeared red in the matrix. Mineralized ECM filled the pores and the matrix mineralization measured by alizarin red assay, where the optical density is directly proportional to calcium-content indicated no significant difference at each time point for all the foam structures (Fig. 19). An increase in calcium-content was observed for all the foam structures and controls until day 21, with significantly higher activity on controls until day 14. The calcium-levels determined on all foam structures and controls were similar at day 21.

## DISCUSSION

We assessed the proliferation and differentiation of preosteoblasts on cellular foam structures and their ability to generate a mineralized bone-like ECM by secreting bone markers (ALP, calcium, etc.) over the ligaments and in the pores. The assessment was carried out in parallel with flat/nonporous Ti alloy and TCP (controls).

The 3D titanium alloy foam structures closely mimic or resemble the microarchitecture (spatial organization of cells and ECM molecules) expected for *in vivo* bone.<sup>17</sup> More importantly, the foam structures provided conditions, which



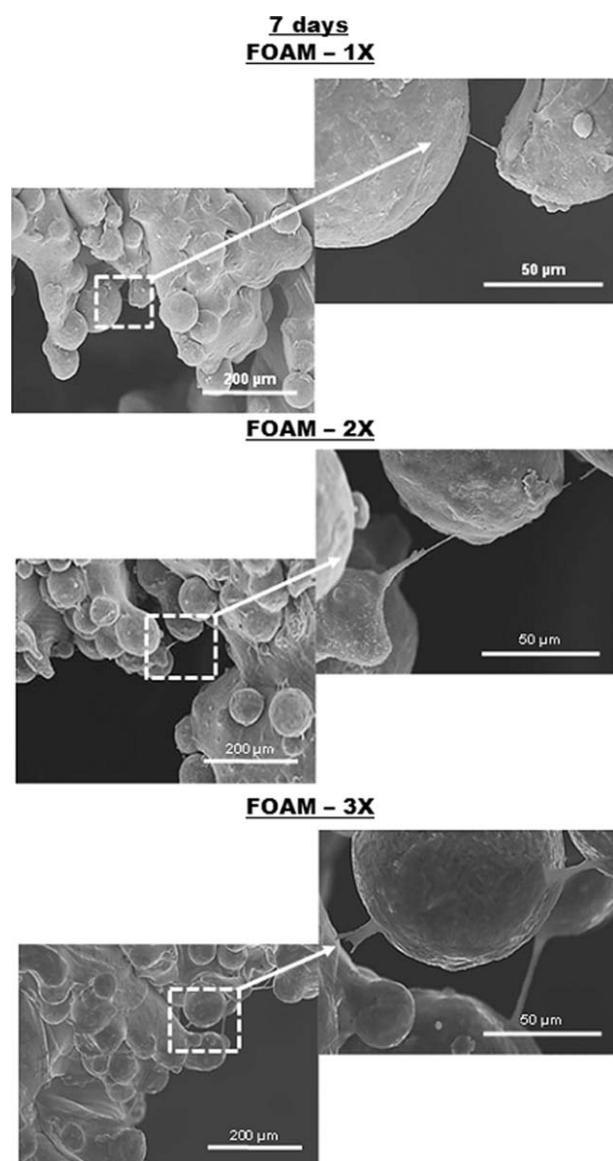


**FIGURE 8.** Low (left) and high (right) magnification scanning electron micrographs representing cellular ingrowth and interconnectivity of preosteoblasts (bridging the pores) on 3D-porous Ti-alloy foam structure with different porosity (Foam 1X: porosity~76%, Foam 2X: porosity~86%, and Foam 3X: porosity~90%), after 7 day incubation period. High magnification areas are indicated by dotted squares in the low magnification images.

were favorable for the synthesis of bone tissue by impacting cell adhesion, spreading, differentiation, and mineralization processes. The interconnected porous architecture of foam structures is beneficial in facilitating circulation of physiological fluid, oxygen, and nutrients, and migration of cells to the core of the biomedical device. From the perspective of long term structural integrity, the migration of cells into the body of the foam is advantageous because of ease in mechanical interlocking, while the porous structure is filled with the tissue and is integrated with the structure.

It appears that the average pore size of the 3D titanium alloy foam structures had no obvious or noticeable impact

on the differentiation and mineralization processes, and influenced only the proliferation stage. The high level of ALP activity observed after day 14 was consistent with the decrease in the proliferation activity. The SEM study of the foam structures indicated deposition of ECM by the differentiating osteoblasts providing greater volume from the 3D architecture.<sup>18</sup> The dense nature of the ECM covering the entire structure at day 21 on foam structures was in agreement with the calcium-content and the range was similar to the solid titanium alloy and TCP (controls).

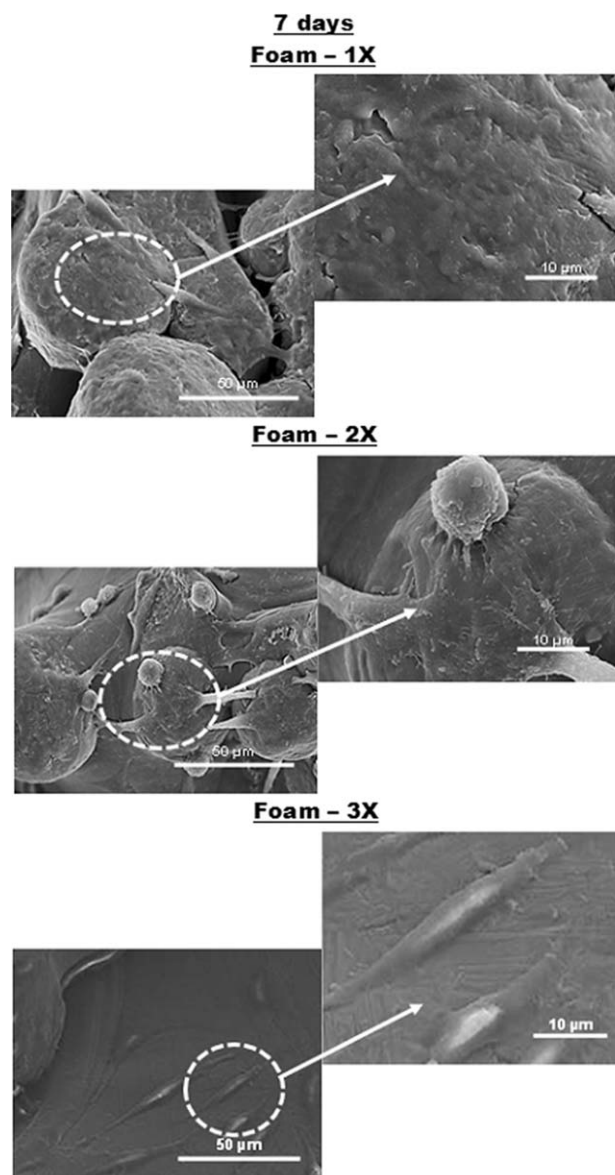


**FIGURE 9.** Low (left) and high (right) magnification scanning electron micrographs representing cell proliferation and spreading of preosteoblasts over the ligament surface of 3D-porous Ti-alloy foam structure with different porosity (Foam 1X: porosity~76%, Foam 2X: porosity~86%, and Foam 3X: porosity~90%), after 7 day incubation period. High magnification areas are indicated by dotted circles in the low magnification images. The proliferated cells showing well-spread morphology on the ligaments were observed to be embedded in the fibrous ECM.

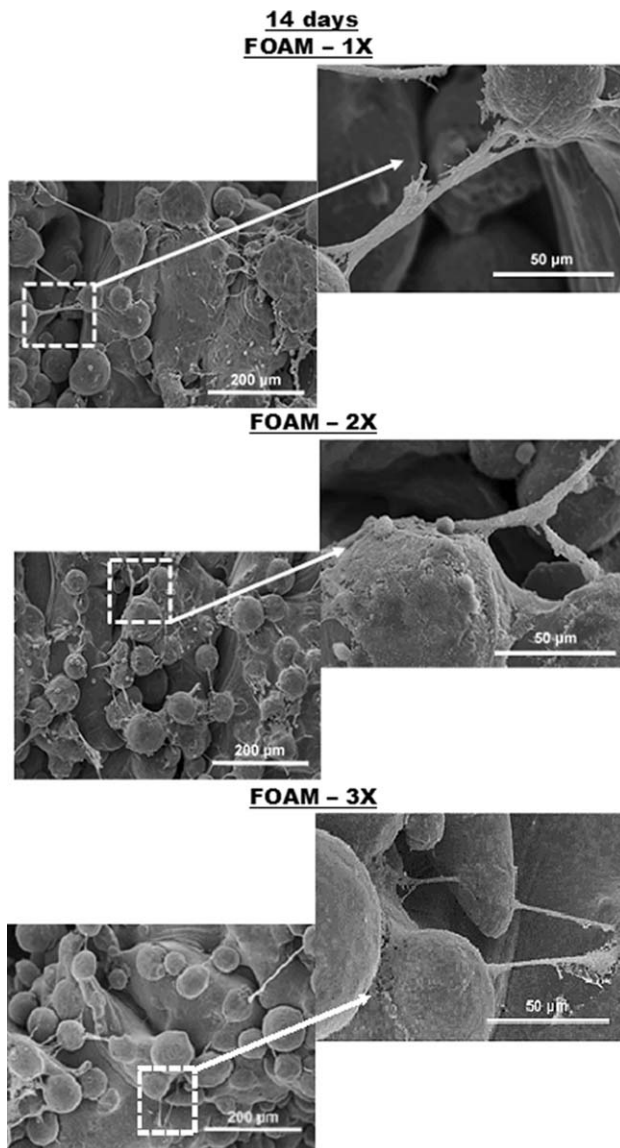


**FIGURE 10.** Low (left) and high (right) magnification scanning electron micrographs representing cellular ingrowth and interconnectivity of preosteoblasts (bridging the pores) on 3D-porous Ti-alloy foam structure with different porosity (Foam 1X: porosity~76%, Foam 2X: porosity~86%, and Foam 3X: porosity~90%), after 14 day incubation period. High magnification areas are indicated by dotted squares in the low magnification images. Intercellular filopodial contacts were observed to be more on the structures.

An apparent distinction between foam structures and controls (solid titanium alloy and TCP) was the cell seeding efficiency (Fig. 2) observed during the initial stages of cell attachment. Less number of cells attached to the foam structures, which is essentially related to the fact that the permeability of cells depends on the porosity. Penetration of cells through the interconnected porous structure enables cells not only to attach to the lower ligaments, but also to the underlying tissue culture wells. Thus, the seeding efficiency was observed to decrease with increase in the degree of porosity for the pore diameter.

The initial cell attachment, viability, and proliferation, as determined by MTT assay on foam structures was significantly different from controls (solid titanium alloy and TCP) [Fig. 3(a,b)]. An increase in the proliferation rate observed in foam structures (Fig. 4) is a consequence of the 3D porous environment that is conducive to the efficient supply of nutrients and penetration of cells into the interconnected porous architecture. Moreover, proliferation of cells after day 7 was qualitatively visible from the fluorescent micrographs, that is, from the stained nucleus of osteoblasts present on the ligaments of the scaffolds (Fig. 5). With progress

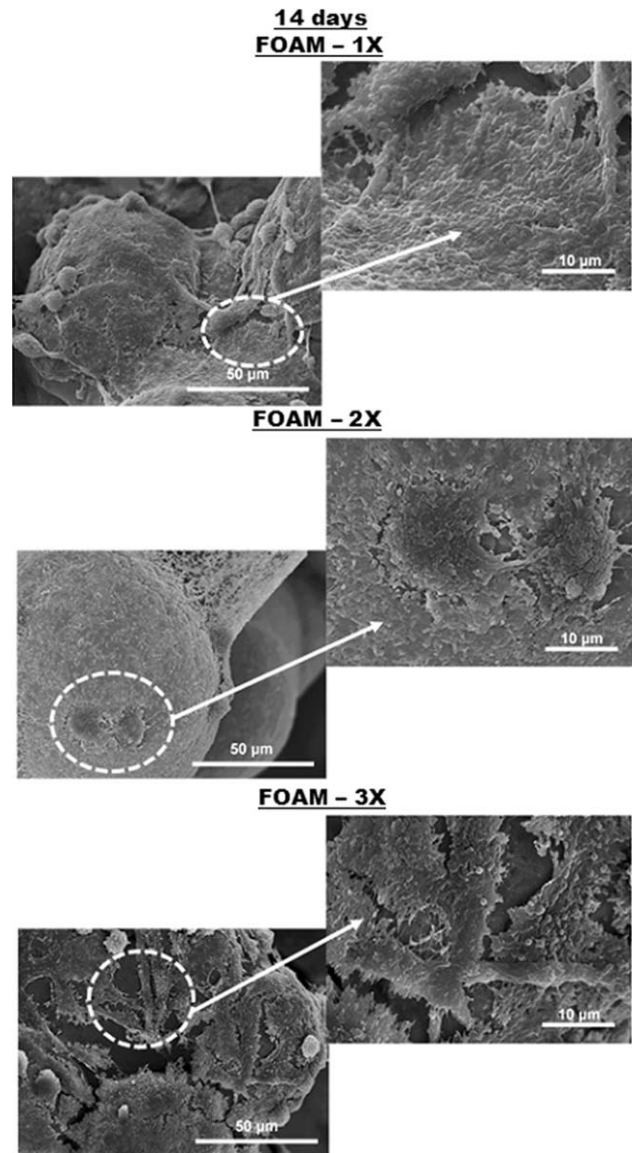


**FIGURE 11.** Low (left) and high (right) magnification scanning electron micrographs representing morphology of preosteoblast cells embedded in ECM over the ligament surface of 3D-porous Ti-alloy foam structure with different porosity (Foam 1X: porosity~76%, Foam 2X: porosity~86%, and Foam 3X: porosity~90%), after 14 day incubation period. High magnification areas are indicated by dotted circles in the low magnification images. The dense ECM secreted by differentiating cells observed to be present all over the ligament surface of the structures.



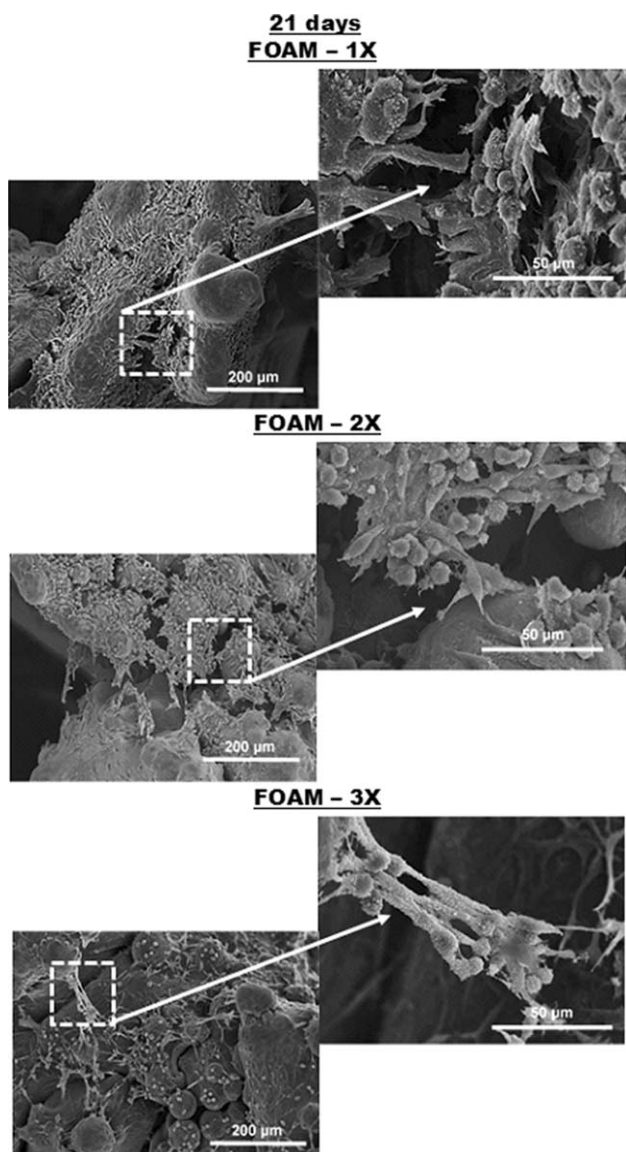


**FIGURE 12.** Low (left) and high (right) magnification scanning electron micrographs representing cellular ingrowth, interconnectivity of pre-osteoblasts (bridging the pores), and mineralized nodules on 3D-porous Ti-alloy foam structure with different porosity (Foam 1X: porosity~76%, Foam 2X: porosity~86%, and Foam 3X: porosity~90%), after 21 day incubation period. High magnification areas are indicated by dotted squares in the low magnification images.

in culture time beyond the proliferation stage, i.e. for up to day 21 (differentiation and mineralization stages), a decrease in metabolic activity was observed on all the test materials, while it implied more significant on controls. These differences were confirmed by the SEM study, which implied that the dense packing of cells in the ECM prevented the dye from reacting with the cells. A similar behavior was reported on earlier occasions,<sup>19,20</sup> where it was shown that the dense ECM network generated by the differentiating osteoblasts prevents complete release of DNA content during cell lysis.

The ECM dictates cell-substrate interactions by playing an important role in signal transduction, where the extracel-

lular events are communicated to intracellular processes by the ECM-transmembrane-cytoskeleton network.<sup>21-23</sup> Thus, in this context, we studied primary ECM proteins that influence cellular activity or tissue growth, notably fibronectin, vinculin, and actin. Vinculin, a protein that is colocalized with focal adhesion contacts behaves as a molecule that forms a bridge between intracellular and extracellular proteins. The ECM protein, fibronectin, is one of the earliest product that is secreted by the osteoblasts<sup>24,25</sup> during cell adhesion and acts as a growth stimulator.<sup>22-25</sup> Other ECM components that are responsible for cell attachment and

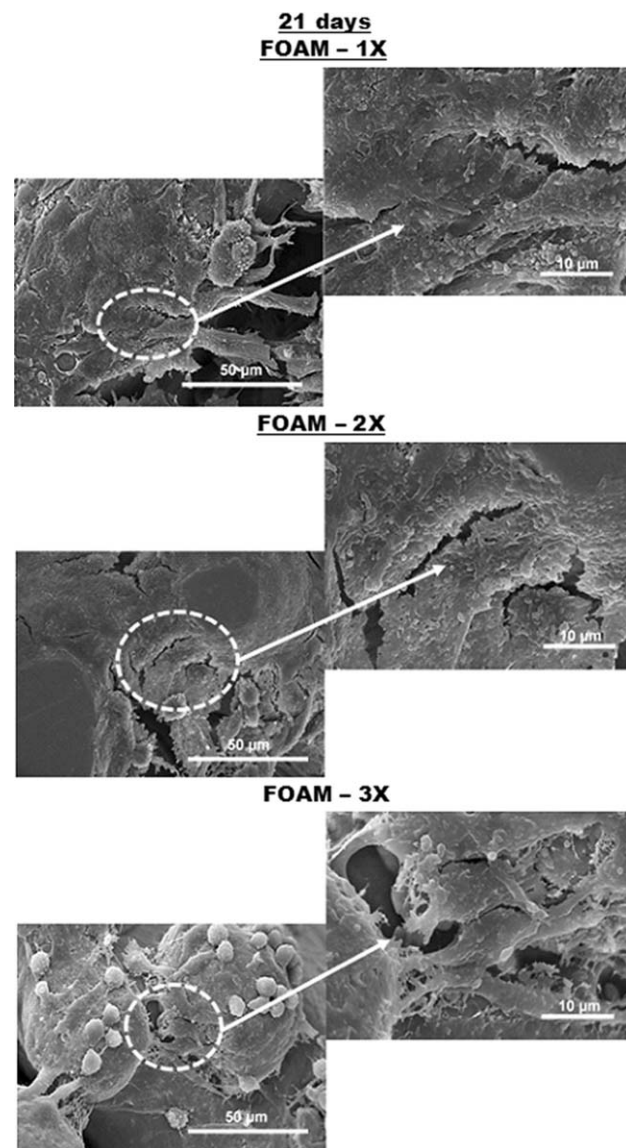


**FIGURE 13.** Low (left) and high (right) magnification scanning electron micrographs representing morphology of preosteoblast cells embedded in ECM over the ligament surface of 3D-porous Ti-alloy foam structure with different porosity (Foam 1X: porosity~76%, Foam 2X: porosity~86%, and Foam 3X: porosity~90%), after 21 day incubation period. High magnification areas are indicated by dotted circles in the low magnification images. The dense ECM secreted by differentiating cells observed to be mineralized and is present all over the ligament surface of the structures.



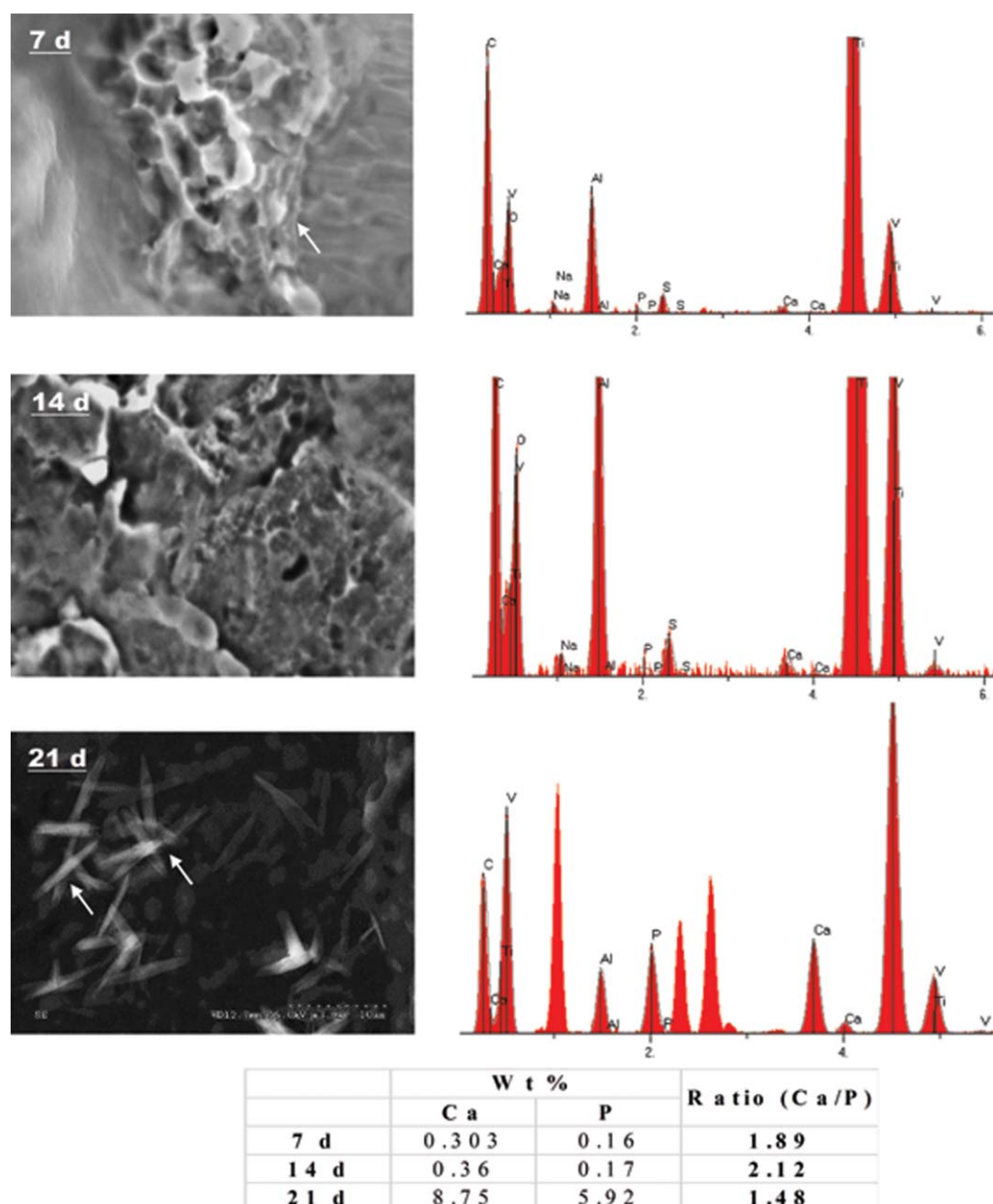


**FIGURE 14.** Scanning electron micrographs (left), and elemental spectrum (right) representing calcium specific mineralized nodules of ECM (white arrows) and elemental composition on 3D-porous Ti-alloy structure after 7, 14, and 21 day incubation periods. The table indicates the ratio of calcium to phosphorous composition reaching that of natural bone-like apatite after 21 d. [Color figure can be viewed in the online issue, which is available at [wileyonlinelibrary.com](http://wileyonlinelibrary.com).]

differentiation are vitronectin and type I collagen. High intensity and uniform distribution of actin, vinculin, and fibronectin observed here in 3D foam structures (Figures 6 and 7) are indicative of superior signal transduction during cell adhesion, in comparison to the controls.

The ability of cells to migrate throughout the interconnected porous structure and form colonies confirmed the natural adaptation of preosteoblasts to the 3D environment.<sup>18</sup> Cells adhered to the ligament with numerous cytoplasmic extensions (Figs. 8–13). The interconnecting porous architecture and the elongated morphology of the cells forming bridge between the pores contributed to the migra-

tion of cells and consequently colonization of the entire structure. It is natural to expect that the intercellular filopodial interactions between neighboring cells contributed to the secretion of ECM, leading to maturation and mineralization with progress in proliferation (Fig. 9).

The colony of cells present in the confluent layer of ECM was observed to form bridges between the pores for day 14 and beyond (21 d). The layer-by-layer organization of cells in the matrix together with the ligaments of the foam structures implied production of osteoid-like matrix.<sup>17</sup> Given, that the mineralized ECM with calcium nodules were present along the ligaments of the foam structures, it is clear

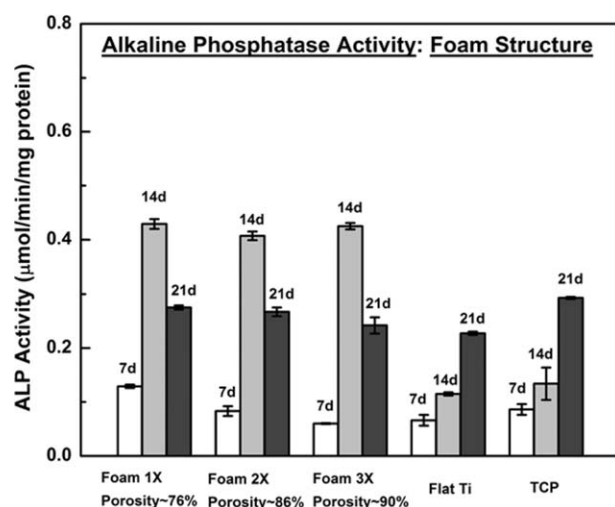


**FIGURE 15.** Histograms representing normalized ALP activity of preosteoblast cell lysates after culture time of 7, 14, and 21 days for flat-Ti, TCP, and cellular Ti-foam 3D-structures of different porosity (Foam 1X: porosity~76%, Foam 2X: porosity~86%, and Foam 3X: porosity~90%). The enzymatic activity is significantly higher on porous scaffolds than on flat-Ti and TCP until day 14 and is not dissimilar at day 21. The activity within the scaffolds is not significantly different at every time point, which indicates that there is no effect of porosity on ALP activity.

that the 3D porous architecture allowed cells to migrate and secrete ECM along the ligaments, which promoted mineralization into bone-like ECM.

Calcium-rich nodules (Fig. 14) implied later stage of differentiation of osteoblasts. The nodules indicated by white arrows in the SEM micrographs in Figure 14 correlated well with the Ca/P ratio. Hydroxyapatite is major constituent of natural bone with Ca/P ratio of ~1.67. The quantitative analysis of EDX spectra yielded Ca/P ratio of ~0.6 for day 7 and ~1.72 for day 21, suggesting the synthesis of bone-like apatite.

The ALP activity is viewed as the marker that represents the early stage of differentiation. The specific activity of this enzyme after proliferation was appreciably higher for the titanium alloy foam structures, when compared with the nonporous titanium alloy and TCP at day 14, and implied the commencement of the differentiation process (Fig. 15). The increase in ALP activity from day 7 to 14 was supported by the SEM observations, which indicated secretion of fibrous ECM, while it matured to a well differentiated state. Moreover, the 3D osteogenic environment provided by the interconnecting porous architecture of foam structures is the underlying reason for the observed differences in ALP activity between foam structures and controls, and the promotion of osteoblasts to a matured phenotype. With progress in culture time beyond the differentiation stage, the onset and progress in mineralization was monitored by the decrease in activity of ALP enzyme. This corresponds to any changes in activity from day 14 to day 21. The process of upregulation and downregulation of bone markers during proliferation, differentiation, and mineralization stages is useful in monitoring the transformation of osteoblasts to a

matured phenotype.<sup>26</sup> The ALP activity, as observed at each time point for different 3D porous structures exhibited almost similar behavior implying that the structure and the pore size range studied had no apparent effect on differentiation.

Calcium, the bone marker for mature osteoblasts, signifies the later stage of differentiation of osteoblasts and represents mineralization. The observed increase in calcium-content (Figs. 16–18) in the matrix is thereby related to the

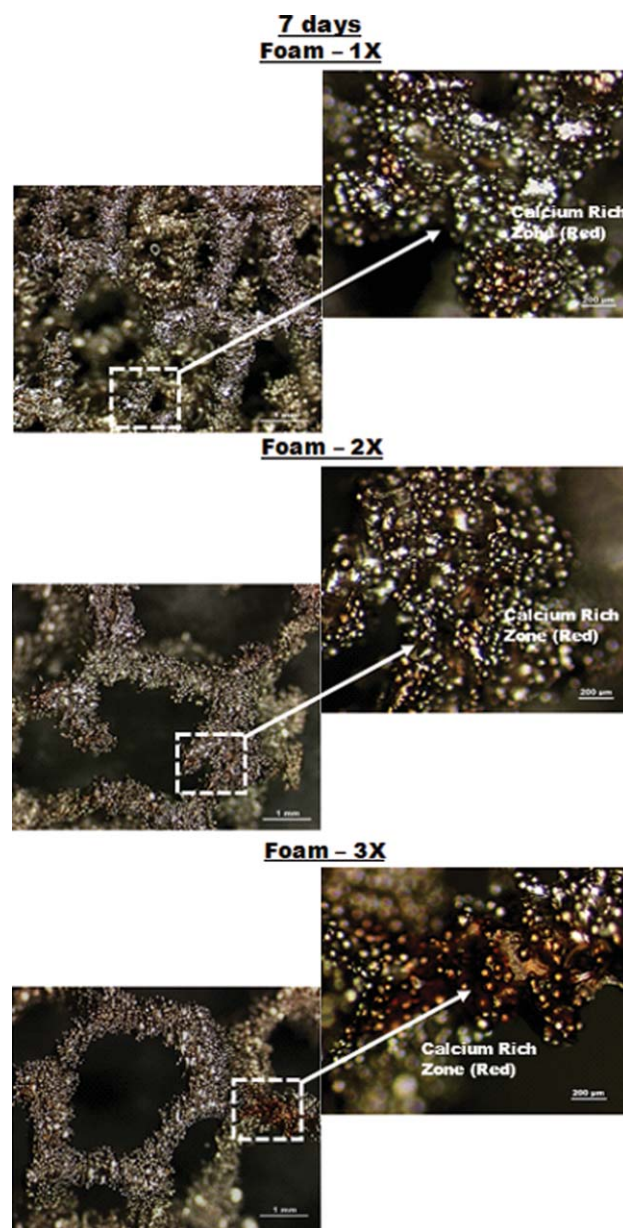


**FIGURE 16.** Low (left) and high (right) magnification optical micrographs of ARS-stained osteoblasts representing mineralization of ECM on 3D-porous Ti-alloy foam structure with different porosity (Foam 1X: porosity~76%, Foam 2X: porosity~86%, and Foam 3X: porosity~90%). High magnification areas are indicated by dotted squares in the low magnification images. Calcium-rich zones (red color portion) on the structures represent the mineralized ECM. [Color figure can be viewed in the online issue, which is available at [wileyonlinelibrary.com](http://wileyonlinelibrary.com).]



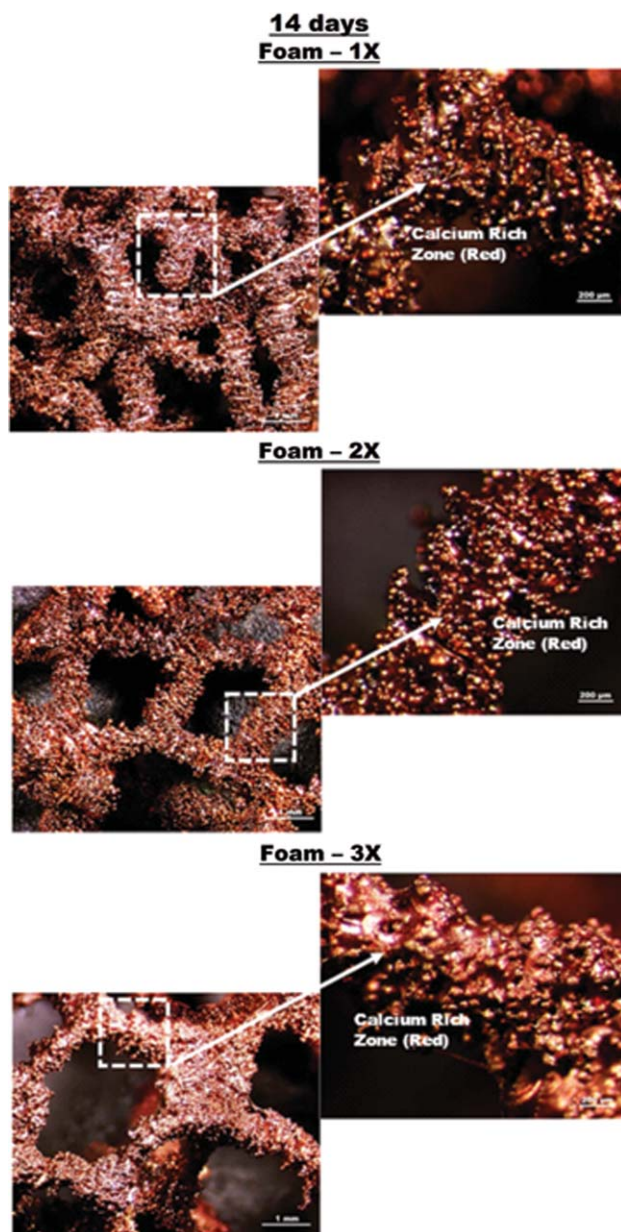


**FIGURE 17.** Low (left) and high (right) magnification optical micrographs of ARS-stained osteoblasts representing mineralization of ECM on 3D-porous Ti-alloy foam structure with different porosity (Foam 1X: porosity~76%, Foam 2X: porosity~86%, and Foam 3X: porosity~90%). High magnification areas are indicated by dotted squares in the low magnification images. Calcium-rich zones (red color portion) on the structures represent the mineralized ECM. [Color figure can be viewed in the online issue, which is available at [wileyonlinelibrary.com](http://wileyonlinelibrary.com).]

ability of osteoblasts to move toward a matured phenotype, consistent with previous studies.<sup>27,28</sup>

In recent years, a number of studies have underscored the relevance of tuning the pore size for effective bone ingrowth.<sup>29–33</sup> Considering that bone tissue ingrowth is also governed by the type of the material, and other factors such as chemical composition of the material, topography, roughness, and interconnectivity of pores, it is reasonable to say

that there are broad range of pore sizes for bone ingrowth to be optimal. In this study, there was no obvious influence of pore size of 3D foam structures on differentiation and mineralization, except that the seeding efficiency and rate of proliferation during the proliferation phase were influenced by the pore size. Even though, irrespective of the fact that the study does not define an optimum pore size for proliferation, differentiation, and mineralization, however, it illustrates a favorable 3D osteogenic microenvironment (spatial

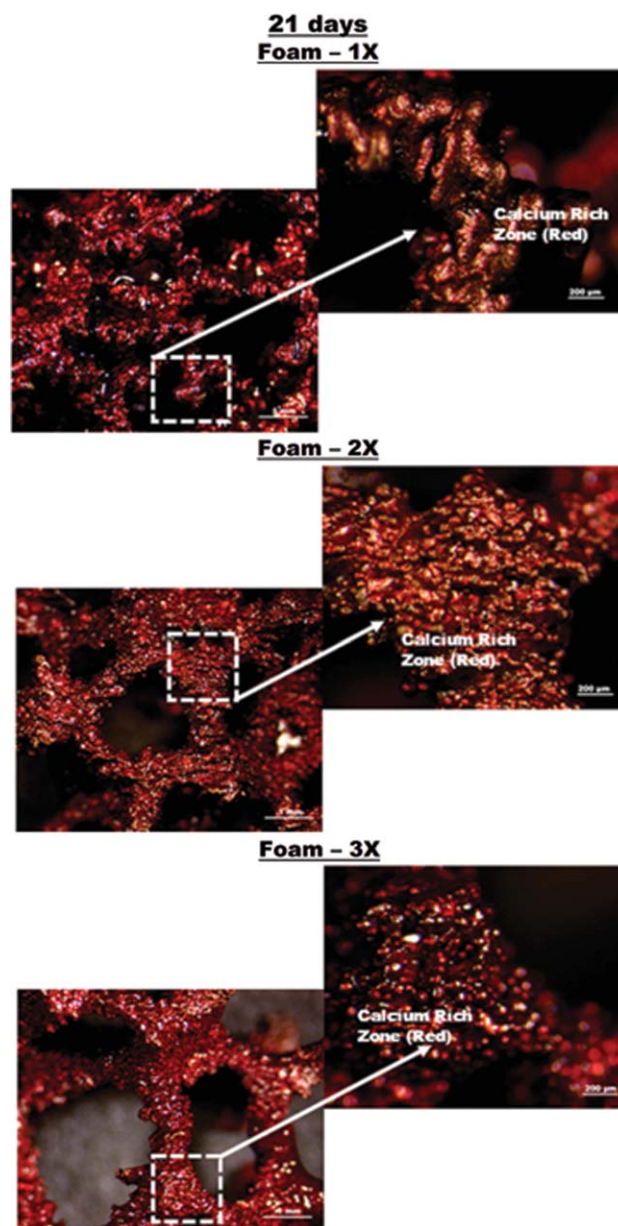


**FIGURE 18.** Low (left) and high (right) magnification optical micrographs of ARS-stained osteoblasts representing mineralization of ECM on 3D-porous Ti-alloy foam structure with different porosity (Foam 1X: porosity~76%, Foam 2X: porosity~86%, and Foam 3X: porosity~90%). High magnification areas are indicated by dotted squares in the low magnification images. Calcium-rich zones (red color portion) on the structures represent the mineralized ECM. [Color figure can be viewed in the online issue, which is available at [wileyonlinelibrary.com](http://wileyonlinelibrary.com).]



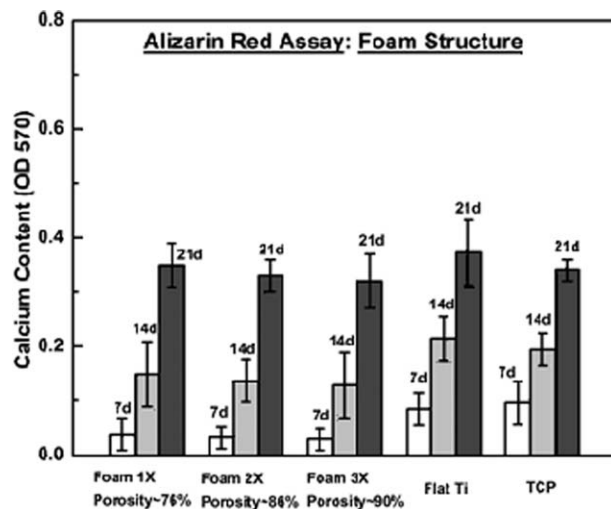


**FIGURE 19.** Histograms representing calcium content in the ECM after culture time of 7, 14, and 21 days for flat-Ti, TCP, and cellular Ti-foam 3D-structures of different porosity (Foam 1X: porosity~76%, Foam 2X: porosity~86%, and Foam 3X: porosity~90%). The optical density is directly proportional to the calcium mineralized in the ECM. The calcium content is significantly higher on flat-Ti and TCP than on porous scaffolds until day 14 and is not dissimilar at day 21. The activity within the scaffolds is not significantly different at every time point, which indicates that there is no effect of porosity on mineralization.

organization of cells and ECM found *in vivo*) that is favorable for bone tissue growth.

In summary, pore diameter and interconnected porous architecture are important and practically relevant determining factors that strongly contribute to bone ingrowth on 3D structures by influencing cell proliferation, differentiation, mineralization, and synthesis of actin, vinculin, and fibronectin. We conclude that the 3D interconnected porous foam-type structure enables mechanical interlocking with the surrounding bone and promotes cell and tissue ingrowth by allowing cells to penetrate into the pores.<sup>34</sup> The favorable biological response of cellular foam structures (with the modulus and pore size varying from ~6-1 GPa and ~700–1500  $\mu\text{m}$ , respectively, in foam), and decrease of mismatch of modulus as addressed in the introduction section, points to the potential of using 3D printed foam structures for bone healing.

## CONCLUSIONS

1. The 3D interconnected porous architecture of foam structures of titanium alloy fabricated via AM was conducive to osteoblast functions (biological response) including cell attachment, proliferation, differentiation, and mineralization, irrespective of low cell seeding efficiency on foam structures.
2. The different pore sizes (700, 1000, and 1500  $\mu\text{m}$ ) of foam structures studied here provided no obvious indications of differences in cellular activity. The similarity in the cellular activity of foam structures is attributed to the 3D osteogenic environment provided by the interconnected porous architecture of foam structures.

3. The highly intense and near-uniform distribution of primary proteins (actin, vinculin, and fibronectin) localizing on ligaments of the foam structures implied signal transduction during cell adhesion and was responsible for the observed superior cellular activity.
4. The 3D foam structures was conducive for cell differentiation at an early stage, a behavior that was in striking contrast to solid titanium alloy and polystyrene culture plates (TCP). Similarly, the ALP activity was appreciably higher on foam structures.
5. Cells adhered to the ligaments of foam structures through formation of numerous cytoplasmic extensions. Intercellular filopodial interaction in foam structures provided a pathway for cell-cell communication and mature to a differentiated phenotype.
6. The ability of osteoblasts to migrate through the interconnected porous architecture resulted in colonization of the entire structure. Cells were embedded layer-by-layer in the ECM with progress in matrix mineralization. During the initial stages of cell proliferation, cells formed a bridge between the pores through elongated extensions. In advanced stages of proliferation, the colony of cells formed a confluent layer of ECM bridging the pores.

## REFERENCES

1. Brunette DM, Tengvall P, Textor M, Thomsen P. Titanium in Medicine: Materials Science, Surface Science, Engineering, Biological Responses and Medical Applications. Berlin: Springer; 2001.
2. Murr LE, Gaytan SM, Medina F, Lopez H, Martinez E, Machado BI, Hernandez DH, Martinez L, Lopez MI, Wicker RB, Bracke J. Next-generation biomedical implants using additive manufacturing of complex, cellular and functional arrays. *Phil Trans R Soc A* 2010; 22:1999–2032.
3. Niinomi M. Mechanical biocompatibilities of titanium alloys for biomedical applications. *J Mech Behav Biomed Mater* 2008;1:30–42.
4. Bronzino JD, editor. The Biomedical Engineering Handbook. Vol. 1, Boca Raton: CRC Press LLC; 2000.
5. Lemmons JE. Inorganic-organic combinations for bone repair. In: Christel P, Meunier A, Lee AJC, editors. *Biological and Biomechanical Performance of Biomaterials*. Amsterdam: Elsevier; 1986. p 51–57.
6. Yang S, Leong KF, Du Z, Chua CK. The design of scaffolds for use in tissue engineering: Traditional factors, Part I. *Tissue Eng* 2001; 7:679–689.
7. Bobyn JD, Stackpool G, Toh KK, Hacking SA, Tanzer M, Krygier JJ. Bone growth characteristics and interface mechanics of a new porous tantalum biomaterial. *J Bone Joint Surg* 1999;81B:907–914.
8. Degischer HP, Kriszt B. Handbook of cellular metals. Weinham, Germany: Wiley-VCH; 2002.
9. Hacking SA, Bobyn JD, Toh KK, Tanzer M, Krugier JJ. Fibrous tissue ingrowth and attachment to porous tantalum. *J Biomed Mater Res* 2002;52:631–639.
10. Bobyn JD, Pillar RM, Binnington AG, Szivek JA. The effect of proximally and fully porous-coated canine hip stem design on bone modeling. *J Orthop Res* 2005;5:393–408.
11. Heintz P, Muller L, Korner C, Singer RF, Muller FA. Cellular Ti-6Al-4V structures with interconnected macro-porosity for bone implants fabricated by selective electron beam melting. *Acta Biomater* 2008;4:1536–1544.
12. Murr LE, Gaytan SM, Medina F, Lopez MI, Martinez E, Wicker RB. Additive layered manufacturing of reticulated Ti-6Al-4V biomedical mesh structures by electron beam melting. In: McGoron AJ, Li CZ, Lin WC, editors. *Proceedings of 25th Southern Biomedical Engineering Conference, ICFMBE Proceedings 24*. New York: Springer, 2009; p 23–28.

13. Murr LE, Gaytan SM, Martinez E, Medina F, Wicker RB. Next generation orthopaedic implants by additive manufacturing using electron beam melting. *Int J Biomater* 2012;Article 245727:1–14.
14. Billiet T, Vandenhaute M, Schelfhout J, Van vlierberghe S, Dubruel P. A review of trends and limitations in hydrogel-rapid prototyping for tissue engineering. *Biomaterials* 2012;33:6020–6041.
15. Malda J, Woodfield TBF, Van der vloodt F, Kooy FK, Martens DE, Tramper J, van Blitterswijk CA, Riesle J. The effect of PEGT/PBT scaffold architecture on oxygen gradients in tissue engineered cartilaginous constructs. *Biomaterials* 2004;25:5773–5780.
16. Hwang CM, Sant S, Masaeli M, Kachouie NN, Zamanian B, Lee SH, Khademhosseini A. Fabrication of three-dimensional porous cell-laden hydrogel for tissue engineering. *Biofabrication* 2010;2:035003.
17. Karageorgiou V, Kaplan D. Porosity of 3D biomaterial scaffolds and osteogenesis. *Biomaterials* 2005;26:5474–5491.
18. Bakar ZA, Hussein BF, Mustapha NM. Cockle shell-based biocomposite scaffold for bone tissue engineering. In: Daniel E, editor. *Regenerative Medicine and Tissue Engineering—Cells and Biomaterials*. Croatia: InTech Open Publishers; 2011. Chapter 17, p 365–390.
19. St-Pierre JP, Gauthier M, Lefebvre LP, Tabrizian M. Three-dimensional growth of differentiating MC3T3-E1 pre-osteoblasts on porous titanium scaffolds. *Biomaterials* 2005;26:7319–7328.
20. Bancroft GN, Sikavitsas VI, van den DJ, Sheffield TL, Ambrose CG, Jansen JA, Mikos AG. Fluid flow increases mineralized matrix deposition in 3D perfusion culture of marrow stromal osteoblasts in a dose-dependent manner. *Proc Natl Acad Sci USA* 2002;99:12600–12605.
21. Garcia AJ, Vega MD, Bioettiger D. Modulation of cell proliferation and differentiation through substrate-dependent changes in fibronectin conformation. *Mol Biol Cell* 1999;10:785–798.
22. Faghihi S, Azari F, Zhilyeav P, Vali H, Tabrizian M. Nanostructuring of a titanium material by high-pressure torsion improves pre-osteoblast attachment. *Adv Mater* 2007;19:1069–1073.
23. Faghihi S, Azari F, Zhilyeav P, Vali H, Tabrizian M. Cellular and molecular interactions between MC3T3-E1 pre-osteoblasts and nanostructured titanium produced by high-pressure torsion. *Biomaterials* 2007;28:3887–3895.
24. Chen LB, Murray A, Segal RA, Bushnell A, Walsh ML. Studies on intercellular LETS glycoprotein matrices. *Cell* 1978;14:377–391.
25. Hynes RO, Bye JM. Density and cell cycle dependence of cell surface proteins in hamster fibroblasts. *Cell* 1974;3:113–120.
26. Ehara A, Ogata K, Imazato S, Ebisu S, Nakano T, Umakoshi Y. Effects of alpha-TCP and beta-TCP on MC3T3-E1 proliferation, differentiation and mineralization. *Biomaterials* 2003;24:831–836.
27. Datta N, Holterf HL, Sikuritsas VI, Jansen JA, Mikos AG. Effect of bone extracellular matrix synthesized in vitro on the osteoblastic differentiation of marrow stromal cells. *Biomaterials* 2005;26:971–977.
28. Sikavitsas VI, Bancroft GN, Lemoine JJ, Liebschner MAK, Dauner M, Mikos AG. Flow perfusion enhances the calcified matrix deposition of marrow stromal cells in biodegradable nonwoven fiber mesh scaffolds. *Ann Biomed Eng* 2005;33:63–70.
29. Hulbert SF, Young FA, Mathews RS, Klawitter JJ, Talbert CD, Stelling FH. Potential of ceramic materials as permanently implantable skeletal prostheses. *J Biomed Mater Res* 1970;4:433–456.
30. Tsuruga E, Takita H, Itoh H, Wakisaka Y, Kuboki Y. Pore size of porous hydroxyapatite as the cell-substratum controls BMP induced osteogenesis. *J Biochem (Tokyo)* 1997;121:317–324.
31. Bobyn JD, Pilliar RM, Cameron HU, Weatherly GC. The optimum pore size for the fixation of porous-surfaced metal implants by the ingrowth of bone. *Clin Orthop* 1980;150:263–270.
32. Ayers RA, Simske SJ, Bateman TA, Petkus A, Sachdeva RL, Gyunter VE. Effect of nitinol implant porosity on cranial bone ingrowth and apposition after 6 weeks. *J Biomed Mater Res* 1999;45:42–47.
33. Itala AI, Ylanen HO, Ekholm C, Karlsson KH, Aro HT. Pore diameter of more than 100 microm is not requisite for bone ingrowth in rabbits. *J Biomed Mater Res* 2001;58:679–683.
34. Story BJ, Wagner WR, Gaiser DM, Cook SD, Rust-Dawicki AM. In vivo performance of a modified CS Ti dental implant coating. *Int J Oral Maxillofac Implants* 1998;13:749–757.